

Molecular Evolution and Star Formation: From Prestellar Cores to Protostellar Cores

Yuri Aikawa

Department of Earth and Planetary Sciences, Kobe University, Kobe 657-8501, Japan

Valentine Wakelam

Université Bordeaux I, LAB, UMR5804, BP 89, 33270 Floirac, France

Robin T. Garrod

Max-Planck-Institut für Radioastronomie, Auf dem Hügel 69, 53121 Bonn, Germany

and

Eric Herbst

*Departments of Physics, Chemistry, and Astronomy, The Ohio State University,
Columbus, OH 43210*

ABSTRACT

We investigate molecular evolution in a star-forming core that is initially a hydrostatic starless core and collapses to form a low-mass protostar. The results of a one-dimensional radiation-hydrodynamics calculation are adopted as a physical model of the core. We first derive radii at which CO and large organic species sublime. CO sublimation in the central region starts shortly before the formation of the first hydrostatic core. When the protostar is born, the CO sublimation radius extends to 100 AU, and the region inside $\lesssim 10$ AU is hotter than 100 K, at which some large organic species evaporate. We calculate the temporal variation of physical parameters in infalling shells, in which the molecular evolution is solved using an updated gas-grain chemical model to derive the spatial distribution of molecules in a protostellar core. The shells pass through the warm region of 10 – 100 K in several $\times 10^4$ yr, and fall into the central star ~ 100 yr after they enter the region where $T \gtrsim 100$ K. We find that large organic species are formed mainly via grain-surface reactions at temperatures of 20 – 40 K and then desorbed into the gas-phase at their sublimation temperatures. Carbon-chain species can be formed by a combination of gas-phase reactions and grain-surface reactions following the sublimation of CH₄. Our model also predicts that CO₂ is more abundant in isolated cores, while gas-phase large organic species are more abundant in cores embedded in ambient clouds.

Subject headings: stars: formation — ISM: molecules — ISM: clouds — ISM: individual (IRAS 16293-2422, L1527)

1. Introduction

In a last decade, great progress has been made in our understanding of the chemical evolution of low-mass star-forming cores (Di Francesco et al. 2007; Bergin & Tafalla 2006, and references therein). Among the observational advances are the detection of chemical fractionation in several prestellar cores; emission lines of the rare isotopes of CO are weaker at the core center than at outer radii, while emission lines of nitrogen-bearing species (e.g., N_2H^+) show relatively good correlation with the centrally-peaked dust continuum (e.g. Caselli et al. 1999; Tafalla et al. 2002).

Theoretical models show that the CO depletion is caused by adsorption onto grains (Bergin & Langer 1997; Aikawa et al. 2001), and that the CO depletion helps to temporarily maintain the N_2H^+ abundance at the core center. Theoretical models also predict that a fraction of the adsorbed CO will be hydrogenated to form H_2CO and CH_3OH on grain surfaces (Allen & Robinson 1977; Hasegawa et al. 1992), which is confirmed by laboratory experiments (Watanabe & Kouchi 2002a; Fuchs et al. 2007). The existence of solid methanol in low-mass star formation regions has been confirmed observationally; Pontoppidan et al. (2003) detected a high abundance of CH_3OH ice (15-25 % relative to water ice) towards three low-mass protostars among ~ 40 observed protostars. Radio observations find gaseous CH_3OH to be abundant in the central regions of protostars (Schöier et al. 2002a). Since the formation of CH_3OH is inefficient in the gas phase (Garrod et al. 2006, 2007), it must be formed by the hydrogenation of CO on grain surfaces in the prestellar core stage, and then sublimated to the gas-phase as the core is heated by the protostar. Although CH_3OH ice is not detected towards the majority of low-mass protostars (Pontoppidan et al. 2003) and the background star Elias 16 (Chiar et al. 1996), the upper limit for the CH_3OH ice abundance is a few % relative to water ice, which is not low enough to contradict the idea that gaseous CH_3OH around protostars is originally formed by grain-surface reactions and then sublimated.

Two major questions, however, remain to be answered, the first being at what stage CO returns to the gas phase. The core remains nearly isothermal as long as cooling by radiation is more efficient than heating by contraction (compression). Eventually, though, the heating overwhelms the cooling, so that the core center becomes warmer. A newly-born protostar further heats the surrounding core. Laboratory experiments show although some fraction of CO can be entrapped in water ice (Collings et al. 2003), a significant amount of

CO sublimates at around 20 K (Sandford & Allamandola 1988). In order to predict if an observable amount of CO returns to the gas-phase during the prestellar core stage or after the birth of a protostar, the temperature distribution in a core should be calculated by detailed energy transfer. Such a prediction is important in order to observe very young protostars. Once it is sublimated, CO again becomes a useful observational probe. In addition, CO sublimation significantly affects the gas-phase chemistry; for example, it destroys N_2H^+ .

The second question concerns how large organic molecules are formed in protostellar cores. In recent years, diverse organic molecules, including methanol (CH_3OH), dimethyl ether (CH_3OCH_3), acetonitrile (CH_3CN), and formic acid (HCOOH), have been detected towards low-mass protostars (Ceccarelli et al. 2007, and references therein). They are still referred to as "hot-core species", because it was once thought that they are only characteristic of hot ($T \sim 200$ K) cores in high-mass star forming regions. A large number of modeling studies on hot-core chemistry show that sublimed formaldehyde (H_2CO) and CH_3OH are transformed to other organic species by gas-phase reactions within a typical timescale of $10^4 - 10^5$ yr (e.g. Millar & Hatchell 1998). In low-mass cores, however, the time scale for the cloud material to cross the hot ($T \sim 100$ K) region should be smaller than 10^4 yr, considering the infall velocity and temperature distribution in the core (Bottinelli et al. 2004a). Furthermore, theoretical calculations and laboratory experiments recently showed that gas-phase reactions are much less efficient in producing some hot-core species, such as methyl formate (HCOOCH_3) and dimethyl ether, than assumed in previous models (Horn et al. 2004; Geppert et al. 2006; Garrod & Herbst 2006).

Several model calculations have been performed on the chemistry that occurs in low-mass protostellar cores. Doty et al. (2004) solved a detailed gas-phase reaction network assuming a core model for IRAS 16293-2422, and succeeded in reproducing many of the observed lines within 50 %. The physical structure of the core; i.e., its density and temperature distribution, was fixed with time. They assumed gas-phase initial molecular abundances that pertain to the high-mass hot-core AFGL 2591. Lee et al. (2004), on the other hand, constructed a core model that evolves from a cold hydrostatic sphere to a protostellar core by combining a sequence of Bonnor-Ebert spheres with the inside-out collapse model by Shu (1977). They solved a chemical reaction network that includes gas-phase reactions along with adsorption and desorption of gas-phase/ice-mantle species. The resulting molecular distributions and line profiles are significantly different from those of the static core models (Lee et al. 2005). The chemical network of Lee et al. (2004), however, does not include large organic species.

In the present paper, we re-investigate molecular evolution in star-forming cores with the partial goal of answering the two questions posed above. We adopt a core model by

Masunaga & Inutsuka (2000); it accurately calculates the radial distribution of temperature, which determines when and where the ice components are sublimated. The model also enables us to follow molecular evolution smoothly from a prestellar core to a protostellar core. The chemistry includes both gas-phase and grain-surface reactions according to Garrod & Herbst (2006); the surface reactions in particular are important for producing organic molecules in a warming environment. Here, we report a solution of the reaction network following the temporal variation of density and temperature in infalling shells to derive a spatial distribution of molecules, including complex organic ones, in a protostellar core.

2. Model

2.1. Physical evolution of a star-forming core

Figure 1 schematically shows the evolution of a star-forming core. As a model for this process, we adopted and partially reran the model calculated by Masunaga & Inutsuka (2000). These authors solved the non-gray radiation hydrodynamics to follow the core evolution from a dense starless (prestellar) core to a protostellar core assuming spherical symmetry. Conservation equations of mass, momentum, and energy were coupled with the frequency-dependent radiation transfer, which was solved by the variable Eddington factor method. Masunaga & Inutsuka (2000) calculated two models with different initial conditions: a homogeneous core (one of uniform density) and a hydrostatic core (a Bonnor-Ebert sphere). We chose the latter one in the present work.

Initially, the central density of the hydrostatic prestellar core is $1.415 \times 10^{-19} \text{ g cm}^{-3}$, which corresponds to a number density of hydrogen nuclei $n_{\text{H}} \sim 6 \times 10^4 \text{ cm}^{-3}$. The outer boundary is fixed at $r = 4 \times 10^4 \text{ AU}$, so that the total mass is $3.852 M_{\odot}$, which exceeds the critical mass for gravitational instability. The temperature in the core is initially $\sim 7 \text{ K}$ at the center and $\sim 8 \text{ K}$ at the outer edge; the cooling by dust thermal emission is balanced with the heating by cosmic rays, cosmic background radiation, and ambient stellar radiation.

In the original model by Masunaga & Inutsuka (2000), the core starts contraction immediately. In the present work, however, we assume that the core keeps its hydrostatic structure for $1 \times 10^6 \text{ yr}$, implicitly assuming that turbulence supports it. This period sets the initial molecular abundances for the collapse stage. After $1 \times 10^6 \text{ yr}$, the core starts to contract. The contraction is almost isothermal as long as the cooling rate overwhelms the compressional heating, but eventually the latter dominates and raises the temperature in the central region. Increasing gas pressure decelerates the contraction and eventually makes the

first hydrostatic core, known as “the first core”, at the center. When the core center becomes as dense as $10^{-7} \text{ g cm}^{-3}$ and as hot as 2000 K, the hydrostatic core becomes unstable due to H_2 dissociation and starts to collapse again (the second collapse). The central density increases rapidly, and within a short period of time the dissociation degree approaches unity at the center. Then the second collapse ceases and the second hydrostatic core; i.e. the protostar, is formed. The protostar is surrounded by the infalling envelope, which we call the protostellar core. After the onset of contraction, the initial prestellar core evolves to the protostellar core in $2.5 \times 10^5 \text{ yr}$. After the birth of the protostar, the model further follows the evolution for $9.3 \times 10^4 \text{ yr}$, during which the protostar grows by mass accretion from the envelope. At each evolutionary stage, the model gives the total luminosity of the core and the radial distribution of density, temperature, and infall velocity at $r \gtrsim 10^{-4} \text{ AU}$. More detailed explanations of core evolution can be found in Masunaga et al. (1998) and Masunaga & Inutsuka (2000).

In the present paper, we report a re-analysis of their results in order to find the sublimation radii of CO and large organic species at each evolutionary stage. We obtained electronic data and the code of Masunaga & Inutsuka (2000) from the author (H. Masunaga), and reran the calculation of the prestellar core phase to increase the number of time steps at which the core structure is recorded. As for the protostellar phase, we used the existing data. We are interested in the region outside 1 AU, which is of importance for radio observations but is not discussed in detail by Masunaga & Inutsuka (2000). Based on this physical core model, we followed the temporal variation of density, temperature, and visual extinction in infalling shells, in which the chemical reaction network was solved (Aikawa et al. 2001, 2005).

2.2. Chemical reaction network

The chemical evolution was computed with the gas-grain model developed in the OSU astrochemical group (Garrod & Herbst 2006). The current version of the model calculates the abundance of 655 species (458 gas-phase and 197 grain-surface atoms and molecules) through a total of 6309 reactions. The model follows the gas-phase as well as the grain-surface chemistry using the rate equation method (e.g. Hasegawa et al. 1992; Ruffle & Herbst 2000). The gas-phase network is based on the osu.2005 database available online (<http://www.physics.ohio-s.edu/~garrod/osu.2005/>) but without the element fluorine, which has been recently added to osu.2005. The model includes chemical reactions that can be important at $T \lesssim 300 \text{ K}$. At the final stage of our core model, the temperature is somewhat higher than this limit at $r \lesssim 10 \text{ AU}$. In the following, we mainly discuss the molecular evolution that occurs at $T \lesssim 300 \text{ K}$.

The assumed elemental abundances, known as “low-metal” values because of their strong

depletions for elements heavier than oxygen, are listed in Table 1. Initially the species are assumed to be in the form of atoms or atomic ions except for hydrogen, which is entirely in its molecular form. The cosmic-ray ionization rate ζ is set to $1.3 \times 10^{-17} \text{ s}^{-1}$.

The neutral species in the gas-phase stick to the grains upon collision with a probability of 0.5. At high temperatures, this probability is much too high. However, since evaporation is so rapid at such high temperatures, it is unimportant what assumption is made. The grain-surface species can evaporate through thermal evaporation and two non-thermal desorption processes. The binding energy of each molecular species on the grain surface is taken from Garrod & Herbst (2006). The first non-thermal mechanism is the action of a cosmic ray encountering a grain, which rapidly increases the grain temperature and allows the evaporation of the species (Hasegawa & Herbst 1993). The second process, as recently developed quantitatively by Garrod et al. (2006, 2007), is based on the assumption that the energy released by exothermic association reactions on grain surfaces can allow the partial evaporation of the products (Williams 1968). In this process, the fraction of product evaporation is given by

$$f = \frac{a(1 - E_D/E_{\text{reac}})^{s-1}}{1 + a(1 - E_D/E_{\text{reac}})^{s-1}}, \quad (1)$$

where E_D is the binding energy of the product, E_{reac} is the energy of formation in the reaction, and s is the number of vibrational modes in the molecule/surface-bond system. The parameter a is the ratio between the surface-molecule bond frequency and the frequency at which the energy is lost to the surface. We assumed an a value of 0.01 for all species based on Garrod et al. (2007). With this value of a , less than 1% of water is evaporated during its formation on grains. Using molecular dynamics calculations, Kroes & Andersson (2006) showed that it is unlikely that this fraction is larger than 1%. If it were, however, only the gas-phase abundances of some large molecules such as CH_3OH would be increased in the outer parts of the protostellar envelope.

Grain-surface species are dissociated by penetrating UV radiation and cosmic-ray induced UV radiation. We note that our model indirectly includes photodesorption via the second non-thermal desorption process discussed above. For example, the photodissociation of water ice produces OH radicals, a fraction of which recombine with hydrogen atoms to re-generate water. Since we assume the partial desorption of the surface-reaction products, UV irradiation of water ice results in desorption of water.

Species can diffuse on the grain surfaces by thermal hopping and react with each other when they meet. No quantum tunneling was assumed even for hydrogen atoms based on recent experimental results (see Garrod et al. 2007, for discussion on this point). Other details concerning the model can be found in Garrod & Herbst (2006) and Garrod et al. (2007).

During the first 1×10^6 yrs of the integration, we computed the chemical abundances under static dense cloud conditions in order to obtain the initial abundances for the collapse. The chemical evolution in infalling shells was then computed as the shells experience temporal variations of density, temperature and visual extinction A_v . Although the original model of Masunaga & Inutsuka (2000) gives the temperatures of gas and dust of various compositions separately, we assumed that the dust temperature is equal to the gas temperature for simplicity.

We calculated the column density of hydrogen nuclei (N_H) from the core outer edge to each shell and converted it to A_v by the formula $A_v = N_H / (1.59 \times 10^{21} \text{cm}^{-2})$ mag. Initially the visual extinction from the outer edge ($r = 4 \times 10^4$ AU) to the core center is about 5.5 mag, and the shells we follow are located at $\sim 1 \times 10^4$ AU, where $A_v \sim 1$ mag. Assuming that our model core is embedded in ambient clouds, we added 3 mag to the visual extinction obtained above, and ignored photodissociation of CO and H₂. In §4, we also report molecular evolution in an isolated core, in which the extra 3 mag is not added to A_v .

3. Results

3.1. Physical evolution of the core and sublimation radius

Figure 2 shows the radial distributions of density, temperature and infall velocity in the model core at assorted evolutionary stages. We define the moment of the protostar formation as $t_{\text{core}} = 0$. The left panels refer to the prestellar phase, which occurs before the birth of the protostar, and the right panels to the protostellar phase. The distributions are shown at different times in each panel.

We concentrate on the region outside 1 AU, which is of importance for radio observations but is not discussed in detail by Masunaga & Inutsuka (2000). At $t_{\text{core}} < -1 \times 10^3$ yr, more than 1×10^3 yr before the formation of a protostar, the core is almost isothermal and the core contraction is similar to the Larson-Penston (L-P) collapse with a constant temperature (Larson 1969). At $t_{\text{core}} \sim -1 \times 10^3$ yr, the core center starts to heat-up, and the core deviates from the L-P core. The increasing pressure decelerates the contraction, and the first hydrostatic core, of radius ~ 1 AU, is formed at $t_{\text{core}} \sim -5.6 \times 10^2$ yr (see the sharp velocity gradient at ~ 1 AU in Figure 2). When the central density and the central temperature reach $n_H \sim \text{several } 10^{17} \text{ cm}^{-3}$ and ~ 2000 K, dissociation of H₂ leads to the second collapse, which ceases in a short time scale (~ 1 yr). In the protostellar stage, the density in the core envelope decreases with time because of the accretion to the central star, while the temperature and infall velocity increase.

In Figure 3, the temperature at the core center through 200 K is plotted as a function of the central density $n_{\text{H}}^{\text{center}}$. The dashed line indicates a temperature of 20 K, which is roughly the sublimation temperature of CO, or the temperature at which the rate coefficients of accretion and thermal desorption for pure CO ice becomes equal. In the prestellar phase, the core temperature is determined by the balance between cooling by thermal radiation and heating by cosmic rays, cosmic background radiation, ambient stellar radiation, and compressional effects. The central temperature for a time decreases to ~ 5 K, because the increasing column density of the cloud prevents the penetration of optical photons. The core temperature starts to rise at $n_{\text{H}}^{\text{center}} \gtrsim 10^6 \text{ cm}^{-3}$, when compressional heating dominates radiative cooling. The temperature increase is, however, rather moderate until the central density reaches $\sim 10^{11} \text{ cm}^{-3}$. Shortly thereafter, CO sublimation starts when the central density reaches a few $\times 10^{11} \text{ cm}^{-3}$. This occurs only several $\times 10^2$ yr before the first-core formation and $\sim 10^3$ yr before the second-core formation.

Figure 4 shows the temporal variation of two radii, inside of which the temperature is higher than 20 K ($r_{20\text{K}}$) and 100 K ($r_{100\text{K}}$). The former is roughly the sublimation temperatures of CO. Desorption energies and thus sublimation temperatures vary among species, but some large organic species such as CH_3OH and HCOOH , which are of current interest, have sublimation temperatures of ~ 100 K. The sublimation radii are plotted as a function of total luminosity of the core instead of the core age, since the former is an observable value. The labels with arrows depict the core age t_{core} . The plot starts about 770 yr before the second-core formation, when the first core is about to be formed. As the first core grows in density, the core luminosity and envelope temperatures increase. At the moment of the second-core formation ($t_{\text{core}} = 0$), $r_{20\text{K}}$ and $r_{100\text{K}}$ are ~ 100 AU and ~ 10 AU, respectively. At the final stage of the model, $t_{\text{core}} = 9.3 \times 10^4$ yr, the total luminosity reaches $\sim 23L_{\odot}$, and the sublimation radii are $r_{20\text{K}} \sim 3.9 \times 10^3$ AU and $r_{100\text{K}} \sim 1.2 \times 10^2$ AU.

3.2. Physical conditions in infalling material

Up to now, we have described the core model with physical parameters that are given as functions of radius at each evolutionary stage, the so-called Eulerian approach. In order to calculate molecular evolution, however, it is more convenient to follow the Lagrangian approach, in which we consider the temporal variation of physical parameters in assorted collapsing shells, because this temporal variation represents the conditions in which the chemical reaction network is solved (Aikawa et al. 2001, 2005).

Figure 5 shows the temporal variation of density and temperature in shells that reach $r = 2.5, 15, 125$ and 500 AU at the final stage of our model ($t_{\text{core}} = 9.3 \times 10^4 \text{ yr} \equiv t_{\text{final}}$).

The infalling shells begin at $r \sim 1 \times 10^4$ AU in the prestellar core, where they stay for 1×10^6 yr, a temporal period omitted in Figure 5. After the core starts contraction, each shell migrates inwards. In the prestellar stage, the variation of density and temperature is not very significant; these shells are at $r \gtrsim 6 \times 10^3$ AU, where the infall velocity is small and the radial gradient of density and temperature is moderate (Figure 2). In the protostellar stage, which occupies a large fraction of Figure 5, they migrate to inner radii where the infall velocity, temperature, and density steeply increase inwards. Hence, the temporal variation of density and temperature accelerate. In order to highlight the rapid variation near and at the final stage, the horizontal axis in Figure 5 is set to be the logarithm of $t_{\text{final}} - t_{\text{core}}$.

A key parameter for the chemistry of hot-core species is the time scale of the hot-core phase and/or, its predecessor, the warm-up phase. In a classical hot-core chemical model, in which the gas-phase reactions of sublimates are followed with a fixed temperature of ~ 200 K, it takes $10^4 - 10^5$ yr to form new large organic species. In other words, the hot-core phase of $10^4 - 10^5$ yr is needed to account for the existence of large organic species (e.g. Millar & Hatchell 1998). In more recent hot-core models, the temperature first increases with time rather than remaining fixed; the warm-up phase is the period in which the temperature rises from 10 K to ~ 100 K. Various reactions occur during the warm-up phase, because many volatile species return to the gas phase, and because the sublimation temperature varies with species (e.g. Viti & Williams 1999). Grain-surface reactions between molecular radicals containing heavy elements are also enhanced in this temperature range (Garrod & Herbst 2006). Considering the formation time scale of stars, Viti et al. (2004) argued that the warm-up phase is longer in stars with lower masses, and estimated the warm-up phase to be 10^6 yr for solar-type stars. Our model, in contrast, gives a warm-up phase of only several 10^4 yr; since the gas and dust are falling inwards towards the central star, the timescale of the warm-up phase is determined not by the time scale of the star formation, but by the size of the warm region divided by the infall velocity. The timescale of the hot-core phase, in which the temperature of the infalling shells is $\sim 100 - 200$ K, is even shorter; the shell reaching $r = 2.5$ AU at t_{final} spends only 100 yr in the region of $T \gtrsim 100$ K before it falls onto the central star. There would thus not be sufficient time for the gas-phase reactions of sublimated species to form complex species. We are dealing here with the formation of a low-mass protostar, so the hot-core stage is more aptly referred to as a “hot corino”, and short time scales have previously been discussed for such regions (Wakelam et al. 2004; Bottinelli et al. 2004a). It should also be noted that in our contracting core model, the central region with high temperatures ($T >$ several tens of K) is continuously fed by infalling materials, which are then lost to the central star.

3.3. Molecular evolution in infalling shells

Figure 6 shows the temporal variation of molecular abundances in the infalling shell that reaches $r = 2.5$ AU at t_{final} . The horizontal axis is again the logarithm of $t_{\text{final}} - t_{\text{core}}$. Black and gray lines represent species in the ice mantle and in the gas phase, respectively. The chemical evolution at $t_{\text{final}} - t_{\text{core}} \leq 4$ yr should be taken with caution because the temperature in the shell exceeds 300 K, while our chemical network is originally constructed for temperatures of $\lesssim 300$ K. The species shown in Figure 6 are mostly (except CO and H) formed by grain-surface reactions. They are desorbed into the gas phase when the shell temperature reaches the sublimation temperature of each species; at this time the fractional abundance of the surface species is simply transferred to a similar fractional abundance in the gas.

Water, the most abundant molecule with a heavy atom, is formed by the hydrogenation of oxygen atoms on a grain surface, and is already abundant when the contraction starts. Methanol, on the other hand, takes longer to reach a high abundance: it is formed by the hydrogenation of solid CO, which occurs efficiently until the shell temperature reaches $\gtrsim 15$ K and the H atom abundance in the ice mantle drops due to evaporation. The fractional abundance of methanol exceeds 10^{-6} at times within 10^5 yr of the final time. Then the abundance reaches a constant value; CH_3OH is constantly destroyed by the cosmic-ray induced photodissociation and re-formed by a low rate of hydrogenation. Solid carbon dioxide is formed by $\text{O} + \text{HCO} \rightarrow \text{CO}_2 + \text{H}$ and $\text{CO} + \text{OH} \rightarrow \text{CO}_2 + \text{H}$. It reaches a fractional abundance of 10^{-5} about 10^4 yr before the final time.

The large organic species are also formed mainly by grain-surface reactions. Dimethyl ether (CH_3OCH_3) and methyl formate (HCOOCH_3) are produced by the surface reactions of the radical H_2COH with CH_3 and HCO , respectively, where H_2COH is formed by hydrogenation of H_2CO . Formaldehyde, at this stage, is constantly formed by hydrogenation and destroyed by a reaction with OH ice and cosmic-ray induced photodissociation. Both CH_3OCH_3 and HCOOCH_3 reach terminal fractional abundances of $\approx 10^{-9}$. Formic acid (HCOOH), on the other hand, is formed by the gas-phase reaction of OH with sublimated H_2CO , after which it is adsorbed onto grains, and remains in the ice mantle until the temperature gets high enough for its sublimation. Its asymptotic fractional abundance is slightly greater than 10^{-8} . Comparing Figure 6 with Figure 5, we can see that these large organic species are mostly produced at temperatures of 20 – 40 K, rather than at $T \gtrsim 100$ K where CH_3OH is sublimated into the gas phase (see also Garrod & Herbst 2006). In this temperature range, heavy-element species such as CO, HCO and CH_3 can diffuse on the grain surface and form complex molecules efficiently.

3.4. Distribution of molecules in a protostellar core

In order to derive the spatial distribution of molecules in the protostellar core, we have calculated molecular evolution in 13 shells, which reach $r = 2.5 - 8000$ AU at t_{final} . Figure 7 shows the radial distribution of (a) physical parameters and (b-d) molecular abundances at t_{final} . Abundances inside 10 AU are not shown for the following two reasons: firstly they are very similar to the abundances at 10 AU, except that the H_2CO abundance drops inwards, and secondly, the temperature in the inner radius is somewhat higher than the temperature range originally considered in our chemical model (§2.2). Figure 7 (b-d) show that large organic molecules are abundant in the gas phase in the central region of the protostellar core. Since they are formed mostly on grain-surfaces, rather than from gas-phase reactions among sublimates, their gas-phase abundances sharply increase at radii corresponding to their own sublimation temperatures and remain high at smaller radii. For example, CH_3CHO extends to ~ 500 AU, while CH_3OH extends to ~ 100 AU. One exception, again, is HCOOH , which extends to ~ 500 AU because of its formation in the gas phase.

Large organic species are abundant in ice mantles at radii of $100 - 1000$ AU. For radii $r \gtrsim 10^3$ AU, the abundances of these species tend to decrease sharply with increasing radius except for methanol. Water, another hydrogen-rich, or saturated, species, remains nearly constant in abundance. In the outer region ($r > 4000$ AU), a large fraction of carbon on the grain surface is in the form of CH_4 (cf. Garrod et al. 2007).

4. Discussion

4.1. Physical structure of the core and sublimation radius

We have re-analyzed and adopted the results of Masunaga & Inutsuka (2000) to derive the sublimation temperatures of CO and large organic species, and to investigate molecular evolution in a star-forming core. The chosen conditions in the envelope can be different from those of other models because the temperature distribution in the envelope depends not only on the evolutionary state and mass of the central object (either the first or second core), but also on the mass distribution in the envelope, which should depend on the initial conditions. Recently, Omukai (2007) investigated the temperature distribution in the first-core envelope assuming mass distributions from the L-P model (Larson 1969) and Shu model (Shu 1977) similarity solutions. The former has a more massive envelope than the latter. When the first core has a mass of $0.05M_{\odot}$, for example, the hydrogen number density at $r = 10$ AU is several 10^{10} cm^{-3} and $\sim 10^9 \text{ cm}^{-3}$ with the L-P model and the Shu model, respectively. The L-P model gives a core luminosity of $10^{-1}L_{\odot}$, and sublimation radii of $r_{20\text{K}} \sim 100$ AU and

$r_{100\text{K}} \sim 10$ AU, while the Shu model yields a core luminosity of $\sim 10^{-3}L_{\odot}$ and an $r_{20\text{K}}$ of ~ 20 AU. The latter model does not exceed 100 K at any radius. Our core model is warmer than the Shu model but colder than the L-P model.

In the second core stage, on the other hand, the envelope structure can deviate from spherical symmetry and be accompanied by a circumstellar disk. Considering a typical angular velocity for molecular cloud cores ($\sim 10^{-14} \text{ s}^{-1}$; e.g., Goldsmith & Arquilla 1985), the centrifugal radius (i.e. the initial disk radius) is ~ 100 AU. Our results at $r \gtrsim$ several hundred AU are thus relatively robust, while the core structure would be significantly different from our model at smaller radii. For example, the large organic species could be sublimated by the accretion shock onto the forming disk rather than in the envelope, since the centrifugal radius ~ 100 AU coincides with the sublimation radius of large organic species in our model.

4.2. Simple molecules

Lee et al. (2004) investigated the evolution of relatively simple molecules, such as HCN and N_2H^+ , in a star-forming core by combining a sequence of Bonnor-Ebert spheres for the prestellar stage with the inside-out collapse model of Shu (1977) for the core after the first-core formation. These simple molecules are often observed in star-forming cores and are of importance as observational probes, while we mainly discussed large organic species in §3. Figure 8 shows the radial distribution of simple molecules in our model at t_{final} .

Comparison with Lee et al. (2004) is not easy because there are many differences in the physical core models and chemical reaction networks. First, the inside-out core model, which is adopted in Lee et al. (2004), yields lower temperatures than our core model, as discussed above. Secondly, we adopt different binding energies for molecules to the grain surface. While the difference is on the order of only a few hundred K for many species, the binding energy of NH_3 is significantly higher in our model (5534 K) than in Lee et al. (2004) (1082 K); the latter value seems to originate from Hasegawa & Herbst (1993), in which the hydrogen bonding of NH_3 is not taken into account. Thirdly, grain-surface reactions, which are the main formation processes of saturated species such as NH_3 and H_2CO in our model, are not included in Lee et al. (2004). Hence, here we compare our results with Lee et al. (2004) qualitatively rather than quantitatively.

A main conclusion of Lee et al. (2004) is that the molecular abundances vary significantly near and inside the CO sublimation radius. For instance, N_2H^+ is destroyed by CO, and thus declines steeply inwards across the CO sublimation radius, an effect which

happens in our model as well. Lee et al. (2004) also found that some molecules, such as H_2CO , have their peak abundance at the sublimation radius; the gas-phase abundance first increases inward via sublimation, but then decreases due to gas-phase reactions at smaller radii. Similar phenomena can be seen in our model, but the spatial variation of the gas-phase abundances is more moderate than in Lee et al. (2004), for which we can think of a few reasons. First, Lee et al. (2004) calculated the molecular evolution in 512 shells, while we calculated the chemistry in only 13 shells. A larger number of shells are needed to resolve abundance fluctuations on a smaller radial scale. Secondly, higher infall speeds, in general, make the abundance distributions more uniform. Since the infall speed is higher at inner radii in the infalling envelope, it would be natural that the molecular abundances remain relatively uniform at $r \lesssim 100$ AU, which is not calculated in Lee et al. (2004). Thirdly, our chemical network includes a much larger number of species and reactions. Lee et al. (2004) used a reduced reaction network with ~ 80 species and ~ 800 reactions to save computational time, while our model includes 655 species and 6309 reactions. In a small reaction network, a sudden increase of a species (e.g., as caused by sublimation) can easily change the abundances of other species through chemical reactions. In a large reaction network, on the other hand, a larger number of reactions contribute to the formation and destruction of each species, and thus the sudden abundance change of one species does not necessarily propagate to other species. Another noticeable difference in our results from those of Lee et al. (2004) is that HCO^+ decreases more steeply inwards at $r \lesssim 1000$ AU in our model; H_3CO^+ and C_3H_5^+ are the dominant positive ions rather than HCO^+ at the inner radii.

The oxygen-bearing species atomic oxygen (O), molecular oxygen (O_2), and gaseous H_2O are also of special interest because O is very reactive and because the two molecules have been intensively observed by the *Submillimeter Wave Astronomy Satellite (SWAS)* and *Odin* Satellite in recent years. Our model predicts that O reaches an abundance of 4×10^{-5} relative to hydrogen nuclei at $r = 8000$ AU, while it steeply decreases inwards from ~ 1000 AU to 100 AU. Even at $r = 8000$ AU, however, H_2O ice is the most abundant O-bearing species (Figure 7). Bergin et al. (2000) summarized the *SWAS* observations of cold molecular clouds by stating that the fractional abundance of O_2 lies under 10^{-6} and that of gaseous water lies in the range 10^{-9} to a few $\times 10^{-8}$. Molecular oxygen has recently been detected towards ρ Oph by *Odin* with an abundance of 5×10^{-8} relative to hydrogen (Larson et al. 2007). These abundances are consistent with our predictions for the outermost radius $r = 8000$ AU, where the density $n_{\text{H}} \sim 10^4 \text{ cm}^{-3}$ and temperature $T < 20$ K are similar to those in molecular clouds.

4.3. Dependence on visual extinction at the core edge

So far we have assumed that the model core is embedded in ambient clouds of $A_v = 3$ mag. In reality, some cores (e.g. Bok globules) are isolated, while others are embedded in clouds. Isolated cores are directly irradiated by interstellar UV radiation, which causes photo-reactions (photodissociation and ionization) in the gas-phase and ice mantles (e.g. Lee et al. 1996; Ruffle & Herbst 2001). In order to evaluate the effect of ambient UV radiation, we recalculated molecular abundances in a core that is directly irradiated by interstellar UV radiation; i.e. $A_v = 0$ mag at the outer edge of the core ($r = 4 \times 10^4$ AU). The photodissociation rates of H_2 and CO were calculated by following Lee et al. (1996), which gives the shielding factors as a function of A_v and column densities of CO and H_2 in the outer radii. The outermost shell for which we calculate molecular evolution is initially located at $r \sim 1.4 \times 10^4$ AU and declines to $r = 8000$ AU at t_{final} . Column densities of CO and H_2 outside of this shell were estimated by assuming $n(\text{CO})/n_{\text{H}} = 5 \times 10^{-5}$ and $n(\text{H}_2)/n_{\text{H}} = 0.5$.

Figure 9 shows the resultant distribution of molecular abundances in a protostellar core at t_{final} . Compared with the embedded core model (Figure 7), the fractional abundances of CH_3OH and H_2CO are lower by more than one order of magnitude, while the CO_2 abundance is higher. When the shells are still at $r \gtrsim$ several thousand AU and have relatively low A_v ($\lesssim 4$ mag), the photodissociation of H_2O ice efficiently produces OH, which reacts with CO to produce CO_2 ice. Methanol in the ice mantle is dissociated to H_2CO , which is further dissociated to CO. Species such as CH_3CHO , HCOOCH_3 and CH_3OCH_3 are also less abundant in the isolated model, because their formation path includes H_2CO in the ice mantle. Formic acid in the gas phase extends only up to ~ 100 AU, while it extends to several hundred AU in the embedded model. In the isolated model, it is formed mainly by $\text{OH} + \text{HCO}$ on the grain surface. Our results may indicate that molecular abundances in hot cores and corinos depend on whether the core is isolated or embedded in clouds.

The importance of photo-reactions on ice mantle abundances has also been investigated in a number of laboratory experiments. For example, Watanabe & Kouchi (2002b) and Watanabe et al. (2007) found that carbon dioxide is efficiently produced by UV irradiation on a binary ice mixture of H_2O and CO, a result that is consistent with our model. However, Watanabe et al. (2007) found that the UV irradiation also produces CH_3OH with a relative abundance of $n(\text{CH}_3\text{OH})/n(\text{CO}) \sim 10\%$ in the ice mixture. Comparison of our model with their experiment is not straightforward because of differences in temperature and included reactions, but we may have underestimated the CH_3OH ice abundance in the irradiated core model. The discrepancy can arise from the H atom desorption rate in our model. We calculated that UV radiation penetrates into the ice mantle and dissociates H_2O to produce

H atoms embedded in ice. Although we do not discriminate between H atoms on the ice surface and those embedded in the ice mantle, the embedded H atoms in reality would have a lower desorption rate and a better chance of reacting with neighboring CO, a reaction that initiates the formation of methanol in the mantles. Discrimination between surface and embedded hydrogen atoms should be included in future work.

4.4. Comparison with observation

Our model results can be compared with observational results of low-mass protostars. Comparison of the physical structure of the core has already been discussed in detail by Masunaga & Inutsuka (2000). Here we concentrate on molecular abundances. First, we compare molecules in ice mantles. The observation of ices towards the low-mass protostar Elias 29 is summarized in Ehrenfreund & Shutte (2000); the abundances of CO, CO₂, CH₃OH and CH₄ relative to water ice are 5.6 %, 22 %, < 4 %, and < 1.6 %, respectively. On the other hand, Pontoppidan et al. (2003) detected a high abundance (15-25 % relative to water ice) of CH₃OH ice towards 3 low-mass protostars among 40 observed protostars. Although the observation of ice features is difficult, it is probable that the composition of ice mantles depends on their environment and the history of the observed regions. From a theoretical point of view, the abundances of molecules on grains and their fractional abundances compared with H₂O ice depend on time and radius from the protostar. In addition, an embedded core and an isolated core lead to significantly different calculated abundances for solid CH₃OH, H₂CO and CO₂.

Table 2 lists ratios of ice species with respect to water ice at t_{final} for local abundances at radii of 1000 AU and 8000 AU and for column densities towards the core center. Since most of the core material exists at $r \leq 8000$ AU along the line of sight, and since the ices are present at $r > 10$ AU, the column density is calculated by integrating the number density of ice species from 10 AU to 8000 AU. It is interesting to note that regardless of the distance from the protostar, the isolated core model gives smaller surface abundances of CH₃OH and H₂CO and a higher surface abundance of CO₂ than the embedded model. In both models, the surface abundance of CO at 1000 AU is much smaller than observed, but it increases towards larger radii up to 10 and 20% in the embedded and isolated models respectively. Comparison with the observations is best done using our column density ratios, which are in reasonable agreement with Elias 29 for both models. Considering the variation among cores, our models show reasonable agreement with observation. The disagreement with CO doubtless results from our assumption concerning desorption rates. In the present work, we use a desorption energy for each species mainly referring to laboratory experiments on

pure ice sublimation or theoretical estimates that sum up the van der Waals forces between adsorbed atoms and grain surface. But in reality, interstellar ice is a mixture, and hence volatile species can be entrapped by less volatile species; recent temperature-programmed desorption results show that in a mixture rich in water ice, much CO desorbs at considerably higher temperatures (Collings et al. 2003).

Table 3 lists the gas-phase abundances of large molecules towards the low-mass protostar IRAS 16293-2422 and in the central region ($r = 30.6$ AU) of our core model. The physical and chemical structures of IRAS 16293-2422 have been intensively studied (Ceccarelli et al. 2000a,b; Schoier et al. 2002b; Cazaux et al. 2003; Chandler et al. 2005). The physical parameters derived by the model at t_{final} ($\sim 23L_{\odot}$ and $r_{100\text{K}} \sim 1.2 \times 10^2$ AU) are very close to the ones of IRAS16293-2422; the observed luminosity of the source is $27 L_{\odot}$ (Walker et al. 1986) and the physical structure has been constrained by multi-line analysis of H_2O and H_2CO observations through a detailed radiative transfer code (Ceccarelli et al. 2000b). It should be noted that the emission lines of large organic molecules observed in this source are not spatially resolved, except for a few lines investigated by interferometric observations (Bottinelli et al. 2004b; Kuan et al. 2004; Remijian & Hollis 2006). The density and temperature of the gas should vary both within the beam and along the line of sight. Hence the derived molecular abundances vary significantly depending on the assumptions concerning the physical structure of the core and the emitting region, which explains the difference in abundances determined by different investigators (see Table 3).

Although it is not obvious which core model, embedded or isolated, should be compared with IRAS16293-2422, we would prefer the embedded core model. While IRAS16293-2422 is in the Ophiuchus molecular cloud, which harbors several UV sources in the form of OB stars, the ^{13}CO and C^{18}O observations indicate that the core is embedded in dense gas (Loren 1989; Tachihara et al. 2000). The high molecular D/H ratios observed towards IRAS 16293-2422 and its neighboring starless core IRAS16293E (Ceccarelli et al. 2007; Vastel et al. 2004) indicate that these cores have been very cold and thus well-shielded from the ambient stellar radiation. Considering the uncertainties in observationally-estimated molecular abundances, HCOOCH_3 , HCOOH , and CH_3CN in our embedded core model show reasonable agreement with the observations. The embedded model, however, underestimates CH_3OCH_3 and overestimates H_2CO and CH_3OH . The isolated core model, on the other hand, reproduces observed abundances of CH_3OH , HCOOH and CH_3CN , but strongly underestimates H_2CO , HCOOCH_3 , and CH_3OCH_3 .

We can think of several possible solutions to improve the agreement with observation. First, it is noteworthy that the gaseous CH_3OH abundance estimated in IRAS 16293-2422 is much lower than the abundance of CH_3OH ice ($n(\text{CH}_3\text{OH ice})/n_{\text{H}} \sim 10^{-5}$, assuming $n(\text{H}_2\text{O}$

ice)/ $n_{\text{H}} \sim 10^{-4}$) detected by Pontoppidan et al. (2003) towards some low-mass protostars. We may have missed or underestimated the reactions which transform CH_3OH to other large organic species. Secondly, the abundances of large organic species in the central region can vary with time. In the present work, we have concentrated on the distribution of molecules only at t_{final} . Shells that reach the central region at different times should experience different temporal variations of physical conditions. Some shells may experience longer periods at $T \sim 20 - 40$ K, where large organic species start to be efficiently formed. This possibility will be pursued in a future work. Thirdly, core models with rotation could produce higher abundances of large organic species; because of the centrifugal force, core material migrates more slowly and stays longer in the temperature range preferable for the formation of large organic molecules (e.g. in a forming disk).

Because of the beam size of the current radio observations, little is known concerning the spatial distribution of the large organic species; they are mostly confined within a few arc seconds from the core center (e.g. Kuan et al. 2004). But there are exceptions; Remijian & Hollis (2006) found that HCOOH and HCOOCH_3 show extended emission of ~ 5 arcsec. Our embedded core model reproduces the extended emission of HCOOH , while HCOOCH_3 is confined to $r < 100$ AU.

4.5. Carbon chains in a protostellar core

Recently, Sakai et al. (2007a) detected strong emission lines of carbon chain species such as C_4H and C_4H_2 towards the low-mass protostar L1527, which is considered to be in a transient phase from class 0 to class I. In general, carbon-chain species are associated with the early stages of a cold cloud core when the dominant form of carbon changes from atomic carbon to CO. Hence, the existence of carbon-chain species towards L1527 is a surprise.

Figure 10 (a-b) shows the temporal variation of CH_4 and carbon-chain abundances in the shell that reaches $r = 2.5$ AU at t_{final} . When the core starts to contract, methane (CH_4) and C_3H_4 are already abundant in ice mantles. Methane has been formed by the hydrogenation of carbon on grain surfaces, while C_3H_4 has been formed by a combination of gas-phase reactions (to form unsaturated carbon chains such as C_3H and C_3H_2) and grain-surface reactions (to hydrogenate them). When the CH_4 sublimates, some fraction reacts with C^+ to form C_2H_3^+ , which is a precursor for ion-molecule reactions that lead to the production of larger unsaturated hydrocarbons. While gas-phase reactions tend to make the carbon chains longer, adsorbed species experience hydrogenation and dissociation by cosmic-ray induced UV radiation. Figure 10 (c-d) shows the distribution of carbon-chain species in our embedded core model. Methane and C_3H_4 are abundant in the ice mantle even at

$r \gtrsim 10^3$ AU, while other hydrocarbons are abundant at a few 100 AU $\lesssim r \lesssim 10^3$ AU. Most of the carbon-chain species desorb at $r \lesssim$ a few 100 AU.

In summary, our model indicates that carbon-chain species can be re-generated in the protostellar core by the combination of gas-phase reactions and grain-surface reactions. It should be noted, however, that large oxygen-containing organic species are not detected in L1527 (Sakai et al. 2007b), while they are abundant in the central region of our model. In future work, the temporal variation of the molecular distribution in model cores should be investigated to see if at certain evolutionary stages carbon-chain species are abundant while large organic species are not. For example, in their recent study of the chemistry of cold cores, Garrod et al. (2007) found that generation of gas-phase hydrocarbons from precursor surface methane occurs at very late times, after the abundance of surface methanol has essentially vanished. More detailed observations are also needed for a quantitative comparison with models. While our model predicts the column density of C_4H to be $2 \times 10^{16} \text{ cm}^{-2}$ towards the central star, the observation gives $2 \times 10^{14} \text{ cm}^{-2}$. The actual column density towards the central star can, however, be larger, because the emission is averaged within the beam (a few 10 arcsec) in the current observation. Methane ice, the precursor of the carbon-chain species in our model, is as abundant as 23 % relative to water ice at the outer edge of our core model. A deep integration of ice features towards field stars is needed to constrain the CH_4 ice abundances at the outer edge of the core and/or quiescent clouds, while the column density ratio of CH_4 ice to H_2O ice (1 %, see Table 2) in our model is consistent with the observation towards YSO’s (§4.3), because of the relatively large sublimation radius of CH_4 .

5. Summary

We have adopted the one-dimensional radiation-hydrodynamical core model of Masunaga & Inutsuka (2000) to investigate molecular evolution in a low-mass star-forming core. The physical structure (density, temperature and infall velocity) of the core is given as a function of time and radius (distance from the core center). The temporal variation of density, temperature and visual extinction is calculated for assorted infalling shells. The temporal variation of molecular abundances in these infalling shells and the radial distribution of molecules in the protostellar core are calculated by solving a chemical reaction network that couples gas-phase and grain-surface chemistry.

In the prestellar phases of star formation, species such as CO, which contain heavy elements, are depleted onto grain surfaces due to low temperatures in the vicinity of 10 K and below. As the contraction proceeds, the compressional heating overwhelms the radiative cooling. When the central density reaches $\sim 10^{11} \text{ cm}^{-3}$, the temperature at the core center

starts to rise sharply and soon reaches the sublimation temperature of CO (~ 20 K). The first hydrostatic core is formed shortly (in several 10^2 yr) thereafter. When the protostar is born, the CO sublimation radius extends to 100 AU, and the temperature at $r \lesssim 10$ AU is higher than 100 K, at which some large organic species start to evaporate.

We investigated the radial distribution of molecules at 9.3×10^4 yr after the birth of a protostar, when the temperature is higher than 20 K and 100 K at $\lesssim 3.9 \times 10^3$ AU and $\lesssim 100$ AU, respectively. The time taken by the infalling shells to warm up from 10 K to 100 K is important for the production of large molecules. We found that this warm-up phase occurs for only several 10^4 yr in our dynamical model. Once the shells enter the region where $T \gtrsim 100$ K, they fall into the central protostar in the very short time of $\sim 10^2$ yr. Large organic molecules such as CH_3OH , HCOOCH_3 and CH_3OCH_3 are formed on grain surfaces at temperatures of 20–40 K and subsequently released into the gas phase by thermal evaporation. In our model, only the abundance of HCOOH seems to be influenced by gas-phase chemistry. As a consequence, the radius at which the gas-phase abundance of an organic molecule typically increases strongly in the envelope corresponds to its sublimation radius. Our model also indicates that carbon-chain species can be formed by a combination of gas-phase reactions and grain-surface reactions after the sublimation of CH_4 .

We compared molecular abundances in an isolated core model, which is exposed to the ambient UV field, and an embedded core model. We found that the photo-reactions in ice mantles are important in determining the ice abundances and thus the molecular abundances in hot corinos. The molecule CO_2 , in particular, is enhanced in the isolated model, while methanol and formaldehyde are more abundant in the embedded model. Our model shows acceptable agreement with gas-phase observations of the hot corino IRAS 16293-2422 and ice-phase observations towards the low-mass protostar Elias 29, considering uncertainties and variations in observed abundances. A more detailed comparison, including a radiative transfer treatment to directly compare with the observed spectra, is desirable.

This work was supported by a Grant-in-Aid for Scientific Research (17039008, 18026006) and by “The 21st Century COE Program of Origin and Evolution of Planetary Systems” of the Ministry of Education, Culture, Sports, Science and Technology of Japan (MEXT). E. H. thanks the National Science Foundation for support of his research program in astrochemistry.

REFERENCES

Aikawa, Y., Ohashi, N., Inutsuka, S.-I., Herbst, E., & Takakuwa, S. 2001, *ApJ*, 552, 639

- Aikawa, Y., Herbst, E., Roberts, H., & Caselli, P. 2005, *ApJ*, 620, 330
- Allen, M. & Robinson, G. W. 1997, *ApJ*, 212, 396
- Bergin, E. A., & Langer, W. D. 1997, *ApJ*, 486, 316
- Bergin, E.A., et al. 2000, *ApJ*, 539, L129
- Bergin, E.A. & Tafalla, M. 2006, *ARA&A*, in press
- Bottinelli, S., Ceccarelli, C. Lefloch, B., Williams, J.P., Castets, A., Caux, E., Cazaux, S., Maret, S., Parise, B., & Tielens, A. G. G. M. 2004, *ApJ*, 615, 354
- Bottinelli, S., Ceccarelli, C., Neri, R., Williams, J.P., Caux, E., Cazaux, S. Lefloch, B., Maret, S., & Tielens, A.G.G.M. 2004, *ApJ*, 617, L69
- Caselli, P., Walmsley, M., Tafalla, M., Dore, L., & Myers, P. 1999, *ApJ*, 523, L165
- Cazaux, E., Tielens, A.G.G.M., Ceccarelli, C., Castets, A., Wakelam, V., Caux, E., Parise, B., & Teyssier, D., 2003, *ApJ*, 593, L51
- Ceccarelli, C., Caselli, P., Herbst, E., Tielens, A.G.G.M., & Caux, E. 2007 in *Protostars and Planets.*, ed. B. Reipurth, D. Jewitt, K. Keil (Tucson: University of Arizona Press), 47
- Ceccarelli, C., Castets, A., Caux, E., Hollenbach, D., Loinard, L., Molinari, S., & Tielens, A. G. G. M. 2000a, *A&A*, 355, 1129
- Ceccarelli, C., Loinard, L., Castets, A., Tielens, A.G.G.M., & Caux, E., 2000b, *A&A* 357, L9
- Chandler, C.J., Brogen, C.L., Shirley, Y.L. & Loinard, L. 2005, *ApJ*, 632, 371
- Chiar, J.E., Adamson, A. J., & Whittet, D.C.B. 1996, *ApJ*, 472, 665
- Collings, M.P., Dever, J.W., Fraser, H.J., McCoustra, M.R.S., & Williams, D.A. 2003, *ApJ*, 583, 1058
- Di Francesco, J., Evans, N. J. II, Caselli, P., Myers, P. C., Shirley, Y., Aikawa, Y., Tafalla, M. 2007, in *Protostars and Planets V.*,ed. B. Reipurth, D. Jewitt, K. Keil, (Tucson: University of Arizona Press), 17
- Doty, S. D., Schöier, F. L., & van Dishoeck, E. F. 2004, *A&A*, 418, 1021

- Ehrenfreund, P., & Shutte, W. A. 2000, in *Astrochemistry: From Molecular Clouds to Planetary Systems*, ed. Y. C. Minh, Y.C. & E. F. van Dishoeck (Chelsea, MI; Sheridan Books; Astronomical Society of the Pacific), 135
- Fuchs, G. W., Ioppolo, S., Bisschop, S. E., van Dishoeck, E. F., & Linnartz, H. 2007, *A&A*, submitted
- Garrod, R. T., & Herbst, E. 2006, *A&A* 457, 927
- Garrod, R. T., Park I-H., Caselli P., & Herbst, E. 2006, *Faraday Discussions*, 133, 51
- Garrod, R. T., Wakelam, V., & Herbst, E. 2007 *A&A*, 467, 1103
- Geppert, W. D., Thomas, R. D., Ehlerding, A. et al. 2006, *Faraday Discuss.* 133, 177
- Gibb, E. L., Rettig, T., Brittain, S., Haywood, R., Simon, T., & Kulesa, C. 2004, *ApJ*, 610, L113
- Goldsmith, P.F. & Arquilla, R. 1985, in *Protostars and Planets II.*, ed. D.C. Black, M.S. Matthews (Tucson: University of Arizona Press), 137
- Hasegawa, T.I., Herbst, E. ,& Leung, C. M. 1992, *ApJS*, 82, 167
- Hasegawa, T. I. & Herbst, E. *MNRAS*, 261, 83
- Horn, A., Møllendal, H., Sekiguchi, O. et al. 2004, *ApJ*, 611, 605
- Kroes, G. J. & Andersson, S. 2006, in *Astrochemistry: Recent Successes and Current Challenges*, ed. D. C. Lis, G. A. Blake, E. Herbst (New York: Cambridge Univ. Press) 427
- Kuan, Y.-J., Juang, H.-C., Charnley, S.B., Hirano, N., Takakuwa, S., Wilner, D.J., Liu, S.-Y., Ohashi, N., Bourke, T.L., Qi, C., & Zhang, Q. 2004, *ApJ*, 616, L27
- Larson, R.B. 1969, *MNRAS* 145, 271
- Larsson, B. et al. 2007, *A&A*, 466, 999
- Lee, H.-H., Herbst, E., Pineau des Forêts, G., Roueff, E., & Le Bourlot, J. 1996, *A&A*, 311, 690
- Lee, J.-E., Bergin, E. A., & Evans, N. J. II 2004, *ApJ*, 617, 360
- Lee, J.-E., Evans, N. J. II , & Bergin, E. A. 2005, *ApJ*, 631, 351

- Loren, R.B. 1989, *ApJ*, 338, 902
- Maret, S., Ceccarelli, C., Caux, E., Tielens, A.G.G.M., Jørgensen, J.K., van Dishoeck, E.F., Bacmann, A., Castets, A., Lefloch, B., Loinard, L., Parise, B. & Schöier, F. L. 2004, *A&A*, 416, 577
- Maret, S., Ceccarelli, C., Tielens, A.G.G.M., Caux, E., Lefloch, B., Faure, A., Castet, A., & Flower, D.R. 2005, *A&A*, 442, 527
- Masunaga, H., & Inutsuka, S. 2000, *ApJ*, 531, 350
- Masunaga, H., Miyama, S. M., & Inutsuka, S. 1998, *ApJ*. 495, 346
- Millar, T. J., & Hatchell J. 1998, *Faraday Discuss.* 109, 15
- Omukai, K. 2007, *PASJ* in press
- Pontoppidan, K. M., Dartois, E., van Dishoeck, E. F., Thi, W. -F., & d’Hendecourt, L. 2003, *A&A*, 404, L17
- Remijian, A.J., & Hollis, J. M. 2006, *ApJ*, 640, 842
- Ruffle, D. P., & Herbst, E. 2000, *MNRAS*, 319, 837
- Ruffle, D. P., & Herbst, E. 2001, *MNRAS*, 324, 1054
- Sakai, N., Sakai, T., & Yamamoto, S. 2007b, *ApSS*, in press
- Sakai, N., Sakai, T., Hirota, T., & Yamamoto, S. 2007a, *ApJ*, in press
- Sandford, S. A., & Allamandola, L. J. 1988, *Icarus*, 76, 201
- Schoier, F. L., Jørgensen, J. K., van Dishoeck, E. F., & Blake, G. A. *A&A*, 390, 1001
- Schöier, F. L., Jørgensen, J. K., van Dishoeck, E. F., & Blake, G. A. 2002, *A&A* 391, 1001
- Shu, F. H. 1977, *ApJ*, 214, 488
- Tachihara, K., Mizuno, A., & Fukui, Y. 2000, *ApJ*, 528, 817
- Tafalla, M., Myers, P. C., Caselli, P., Walmsley, C. M., & Comito, C. 2002, *ApJ*, 569, 815
- Vastel, C., Phillips, T.G., Yoshida, H. 2004, *ApJ*, 606, 127
- Viti, S., & Williams, D. A. 1999, *MNRAS*, 305, 755

- Viti, S., Collings, M. P., Dever, J. W., McCoustra, M. R. S., & Williams, D. A. 2004, MNRAS, 354, 1141
- Wakelam, V., Caselli, P., Ceccarelli, C., Herbst, E., & Castets, A. 2004, A&A, 422, 159
- Walker, C. K., Lada, C.J., Young, E.T., Maloney, P.R., & Wilking, B.A. 1986, ApJ, 309, L47
- Watanabe, N., & Kouchi, A. 2002a, ApJ, 571, L173,
- Watanabe, N., & Kouchi, A. 2002b, ApJ, 567, 651
- Watanabe, N., Mouri, O., Nagaoka, A., Kouchi, A., & Pirronello, V. 2007, ApJ, in press
- Williams, D.A. 1968, ApJ, 151, 935

Table 1: Elemental abundances with respect to H.

Element	Abundance
He	9.75(-1) ^a
N	2.47(-5)
O	1.80(-4)
C ⁺	7.86(-5)
S ⁺	9.14(-8)
Si ⁺	2.74(-9)
Fe ⁺	2.74(-9)
Na ⁺	2.25(-9)
Mg ⁺	1.09(-8)
P ⁺	2.16(-10)
Cl ⁺	1.00(-9)

^a $a(-b)$ means $a \times 10^{-b}$.

Table 2: Percentage abundances of ice-mantle species compared with H₂O ice in model cores at t_{final} . For each core model, ice abundance at radius of 1000 AU and 8000 AU are listed. Ratios of column densities integrated towards the core center are also listed as "column".

Species	Embedded core			Isolated core		
	1000 AU ^a	8000 AU	column	1000 AU	8000 AU	column
CO	7×10^{-11}	10	0.4	8×10^{-9}	23	0.04
CO ₂	10	4	4.2	125	21	45
H ₂ CO	6	3	1.5	2×10^{-6}	0.08	0.03
CH ₃ OH	3	2	2.7	0.1	0.04	0.2
CH ₄	3×10^{-9}	23	1	2×10^{-9}	5	0.4

^aradii

Table 3: Gas-phase molecular abundances in IRAS 16293-2422 and model results.

Species	IRAS 16293-2422	model ^a	
		embedded	isolated
H ₂ CO	1.0(-7) ^b , 1.1(-7) ^c	2.8(-6)	1.3(-11)
CH ₃ OH	1.0(-7) ^d , 9.4(-8) ^c	3.0(-6)	8.5(-8)
HCOOCH ₃	2.5-5.5(-7) ^e , 2.6-4.3(-9) ^f , > 1.2(-8) ^g	1.8(-9)	3.2(-11)
HCOOH	6.2(-8) ^e , 2.5(-9) ^g	1.7(-8)	2.1(-8)
CH ₃ OCH ₃	2.4(-7) ^e , 7.6(-8) ^c	3.5(-10)	5.8(-12)
CH ₃ CN	1.0(-8) ^e , 7.5(-9) ^h	3.0(-8)	1.3(-8)

^aGas-phase abundances at $r = 30.6$ AU are listed, because the abundances are mostly constant at $r \lesssim 100$ AU.

^bMaret et al. (2004)

^cChandler et al. (2005)

^dMaret et al. (2005)

^eCauzax et al. (2003)

^fKuan et al. (2004)

^gRemijian & Hollis (2006)

^hSchöier et al. (2002a)

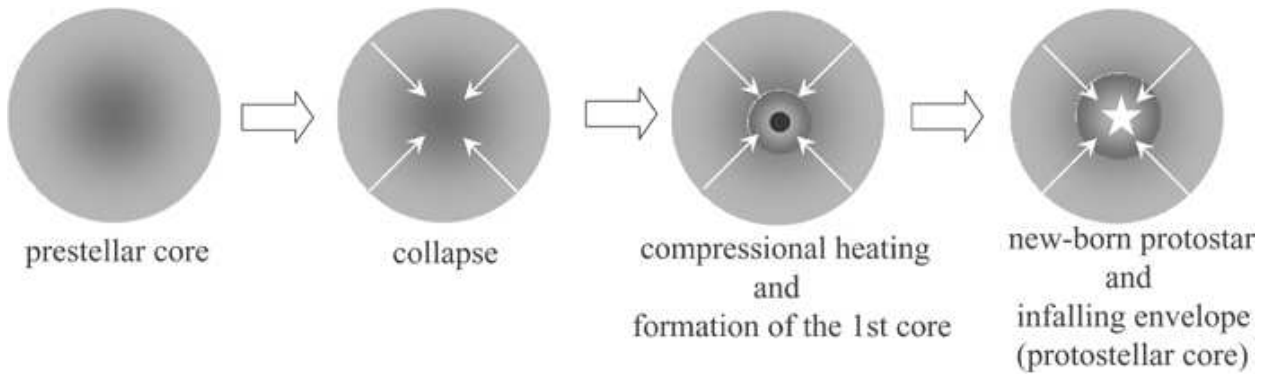


Fig. 1.— Evolution of a star-forming core

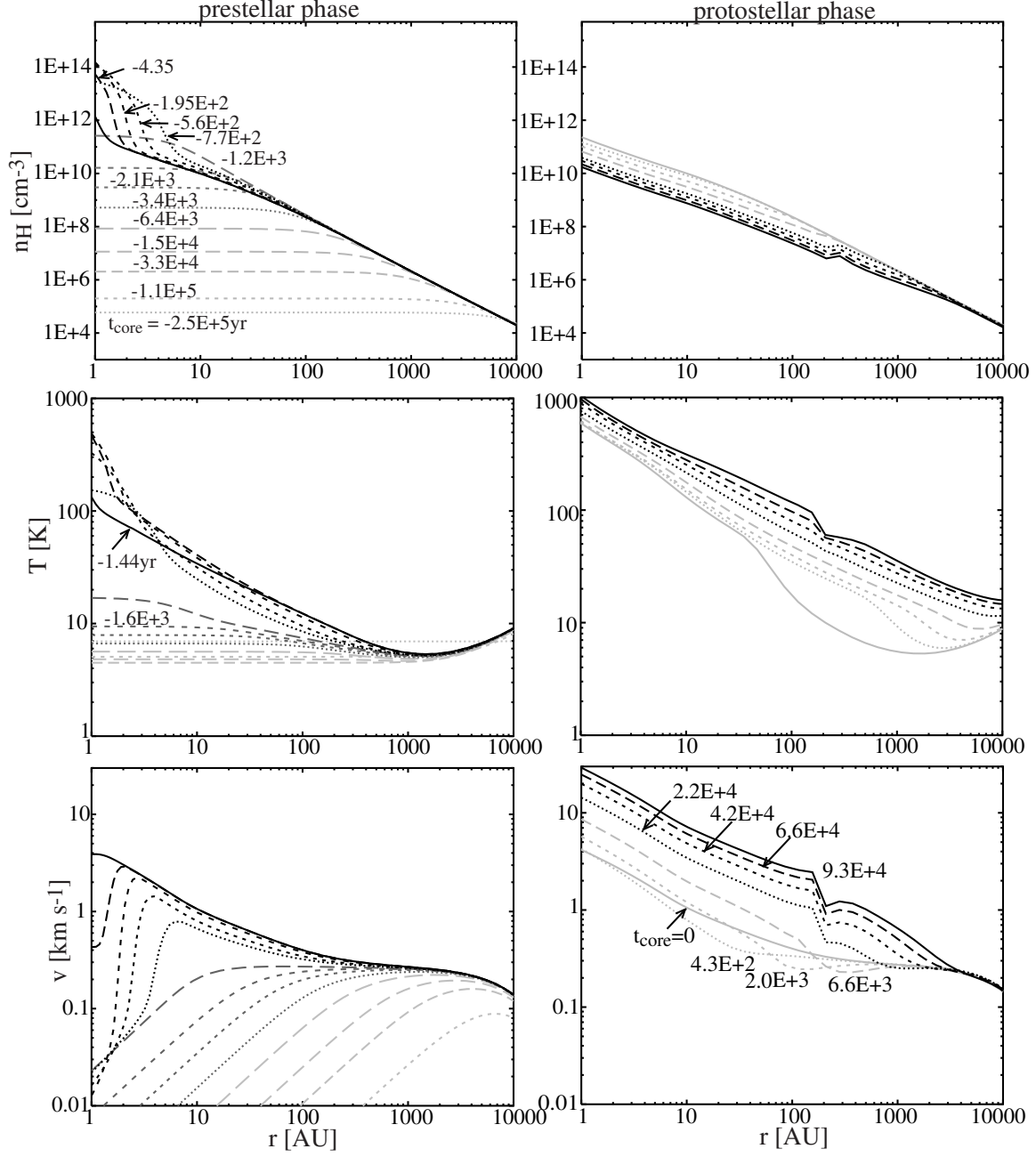


Fig. 2.— Radial distributions of density, temperature and infall velocity in the prestellar core (left panels) and protostellar envelope (right panels). The times shown are relative to the birth of the second hydrostatic core, the protostar.

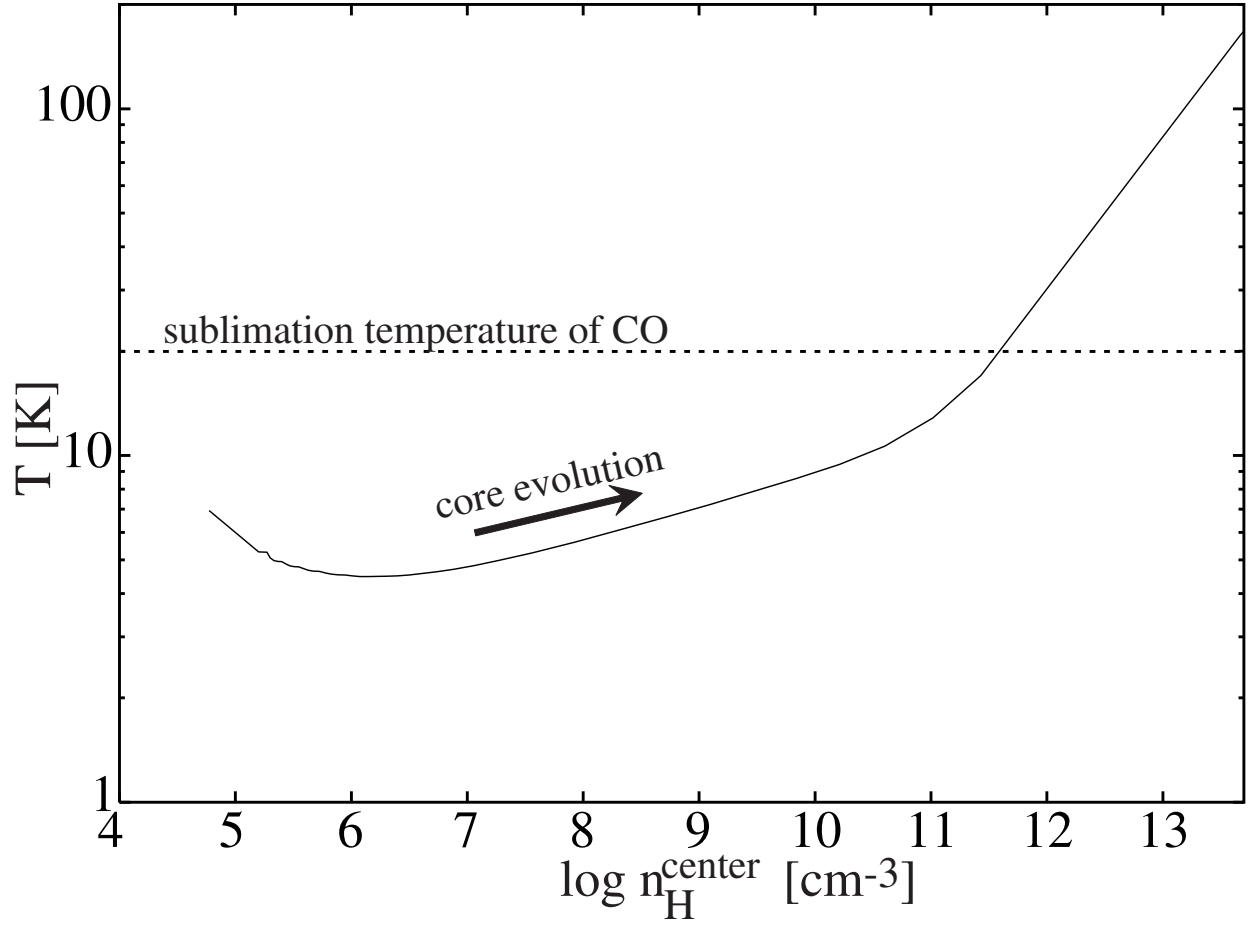


Fig. 3.— Temporal variation of the central temperature of the prestellar core plotted as a function of the central density.

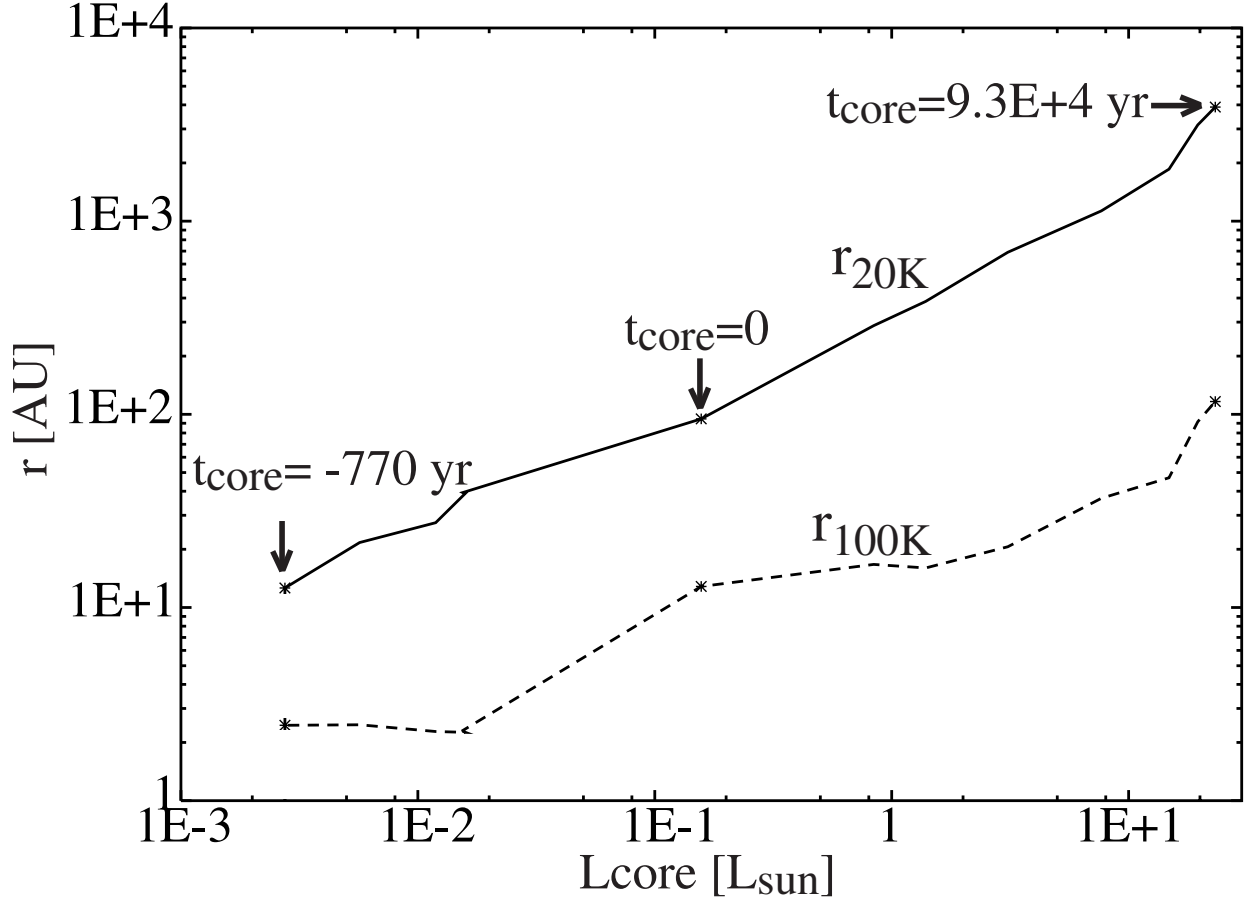


Fig. 4.— Sublimation radius of CO ($r_{20\text{K}}$) and large organic species ($r_{100\text{K}}$) as a function of total luminosity of the core. The solid and dashed lines depict the radius inside of which the temperature is higher than 20 K and 100 K, respectively.

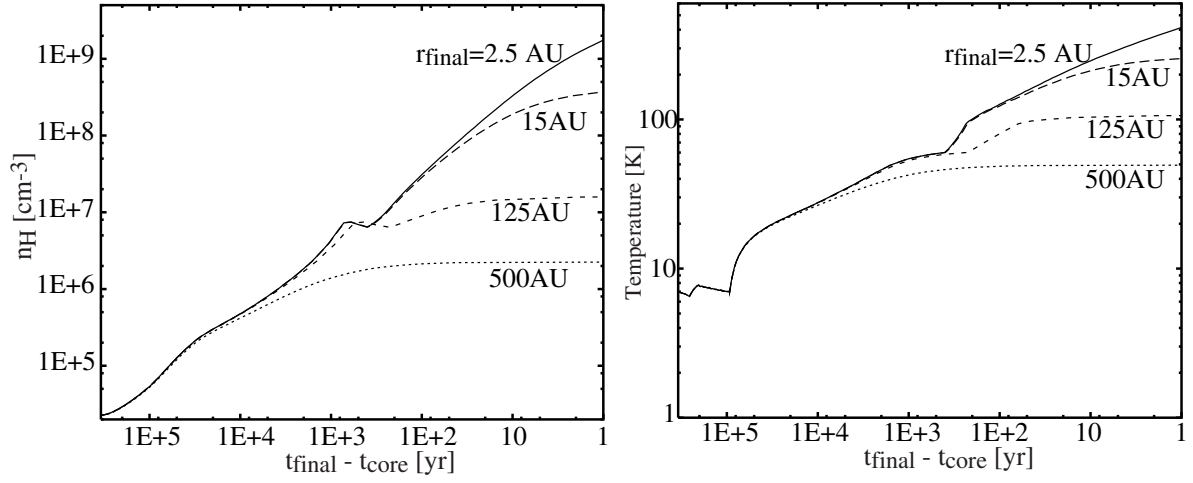


Fig. 5.— Temporal variation of density and temperature in infalling shells that reach $r = 2.5, 15, 125$ and 500 AU at the final stage of our model ($t_{\text{core}} = 9.3 \times 10^4$ yr). The horizontal axis is the logarithm of $t_{\text{final}} - t_{\text{core}}$.

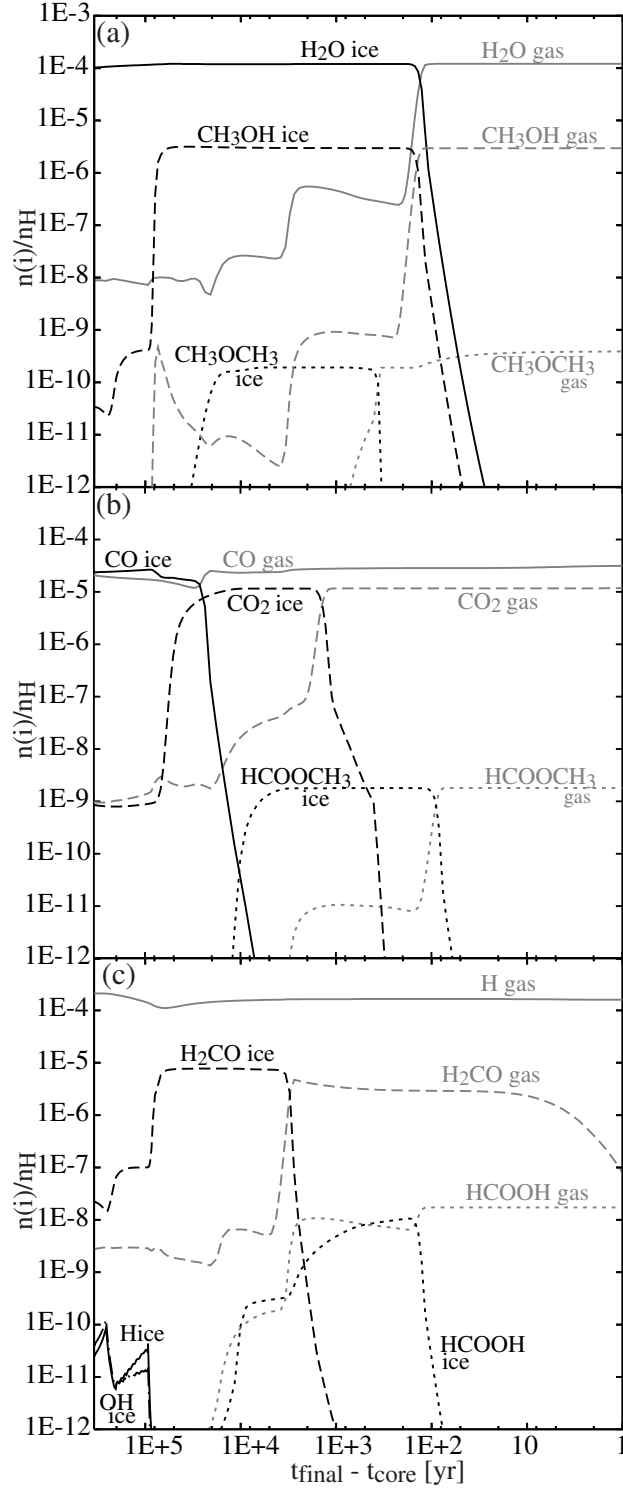


Fig. 6.— Temporal variation of molecular abundances in the shell that reaches $r = 2.5$ AU at t_{final} . The horizontal axis is the logarithm of $t_{\text{final}} - t_{\text{core}}$. Black lines represent ice mantle species, while grey lines represent gas-phase species.

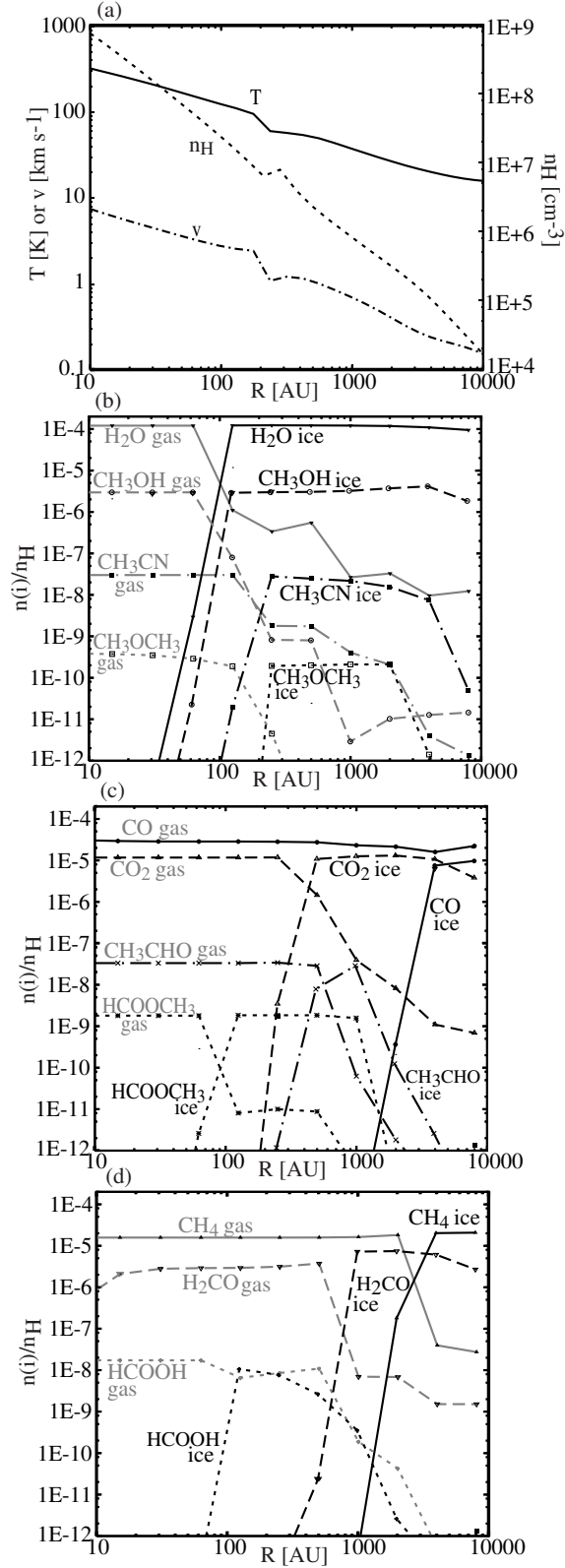


Fig. 7.— Radial distribution of (a) physical parameters and (b-d) molecules in the protostellar core at t_{final} . Black lines represent ice-mantle species, while gray lines represent gas-phase species.

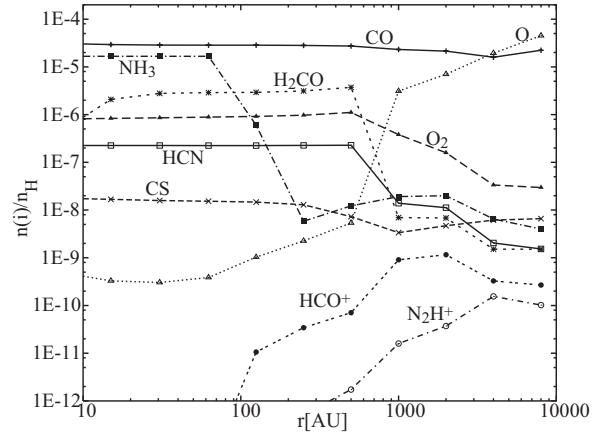


Fig. 8.— Radial distribution of simple gaseous molecules at t_{final} .

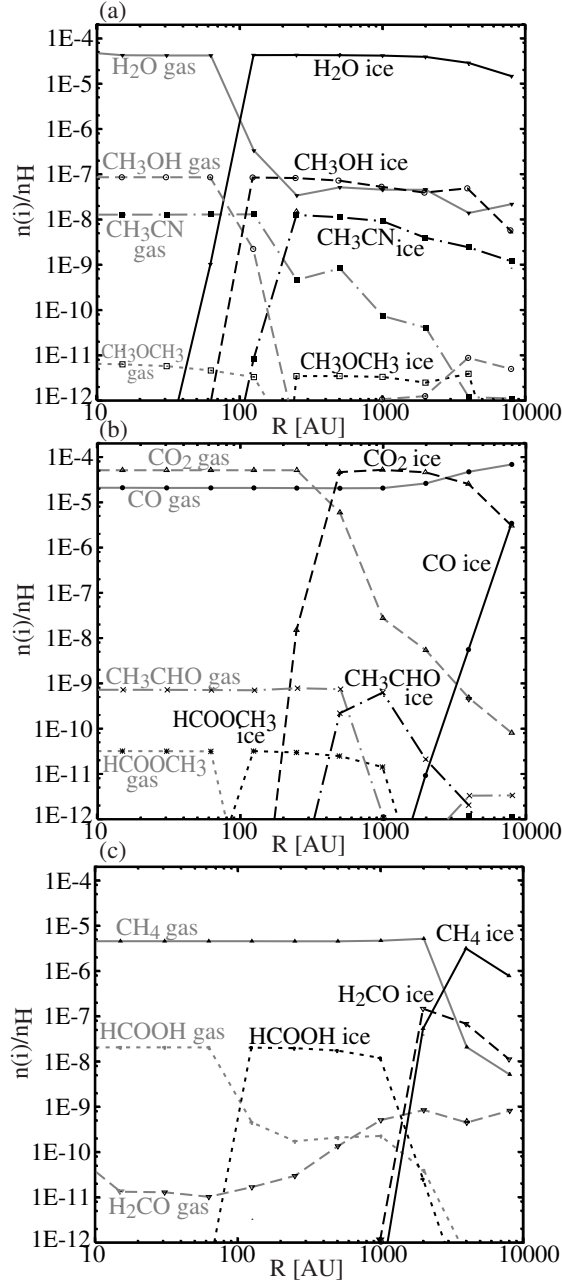


Fig. 9.— Radial distribution of molecules in the protostellar core, as in Figure 7 (b-d). The core is assumed to be directly irradiated by the interstellar UV radiation.

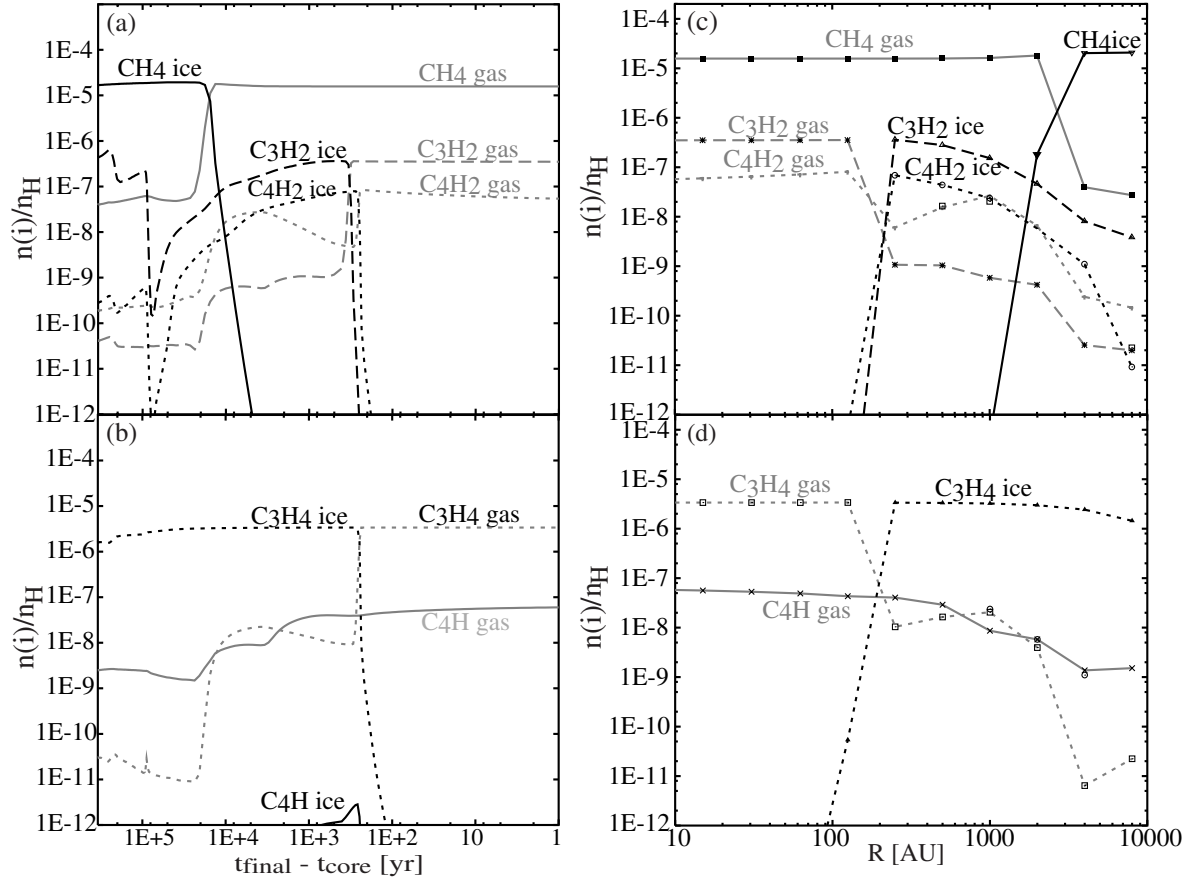


Fig. 10.— (a-b) Temporal variation of carbon-chain abundances in the shell that reaches $r = 2.5$ AU at t_{final} , as in Figure 6. (c-d) Radial distribution of carbon-chain species in the protostellar core, as in Figure 7.